Carbon 185 (2021) 709–716

Contents lists available at ScienceDirect

Carbon

journal homepage: www.elsevier.com/locate/carbon

Research Paper

All-graphene perfect broadband THz absorber

Marian Baah [a, 1], Alesia Paddubskaya [b, 1], Andrey Novitsky [b, c], Nadzeya Valynets [b], Mukesh Kumar [a], Tommi Itkonen [a], Markku Pekkarinen [a], Ekaterina Soboleva [d], Erkki Lahderanta [d], Maria Kafesaki [e, f], Yuri Svirko [a], Polina Kuzhir [a, b, *]

[a] Department of Physics and Mathematics, Institute of Photonics, University of Eastern Finland, P.O. Box 111, FI-80101, Joensuu, Finland
[b] Institute for Nuclear Problems of Belarusian State University, Bobruiskaya Str. 11, 220006, Minsk, Belarus
[c] Department of Theoretical Physics and Astrophysics, Belarusian State University, Nezavisimosti Av.4, 220030, Minsk, Belarus
[d] Lappeenranta-Lahti University of Technology LUT, Yliopistonkatu 34, 53850, Lappeenranta, Finland
[e] Institute of Electronic Structure and Laser, FORTH, 70013, Heraklion, Crete, Greece
[f] Department of Materials Science and Technology, University of Crete, 70013, Heraklion, Crete, Greece

ARTICLE INFO

Article history:
Received 4 August 2021
Received in revised form
3 September 2021
Accepted 29 September 2021
Available online 2 October 2021

Keywords:
Graphene
Metasurface
Terahertz
Perfect absorption
Broadband
Dark plasmon

ABSTRACT

By combining the 3D printing, electroplating and chemical vapor deposition processes we fabricated "bubble wrap" polymer nanomembrane covered with multilayered graphene. Such a metasurface composed of array of graphene hemispheres shows extremely broadband and almost perfect absorption in terahertz (THz)[2] frequency range being robust against macroscopic structural defects including holes and volcanic-like hats on hemispherical metaatoms. The developed theory perfectly explains our experimental findings including virtual independence of the metasurface transmittivity, reflectivity and absorptivity on the angle of incidence in terms of the plasmon dark mode formation. Our approach enables the THz perfect absorber that covers a frequency range spanning from few hundreds of GHz to 1.2 THz, and even more, while the proposed fabrication technique can also be employed in numerous applications that require free standing corrugated graphene/polymer nanomembranes.

1. Introduction

Classical electrodynamics says [1] that if a conductive film is much thinner than the skin depth, it is capable to absorb up to 50% of electromagnetic (EM) radiation. This golden rule remains valid for terahertz (THz) radiation hitting the graphene sheet sandwiched in between polymer layers [2]. Moreover, the THz absorption ability of graphene can be enhanced up to nearly 100% by placing it onto an epsilon-near zero [3] or quarter wavelength thick dielectric substrates [4] that provide a free space impedance matching condition. Alternatively, one can drastically improve absorptivity by adding a back reflector separated from graphene by a dielectric layer [5] that enables constructive interference of the incident and reflected waves in the graphene sheet plane. However, exploring the graphene support for enhancement of the THz absorption is possible only in a relatively narrow frequency range, and requires at least few tens of microns-thick substrate. The latter imposes severe limitations on using graphene in many practical tasks including development of the ultrasensitive ultra-light and ultra-fast bolometers [6,7] that require the unsupported graphene. Extension of the absorption band of the free-standing graphene can be achieved if one "corrugates" the graphene sheet by transforming it into quasi-2D photonic crystal capable to provide nearly zero reflection. In this case one may expect perfect absorption at multiple resonance bands governed by the characteristic size and period of the graphene sheet corrugations.

In this paper we demonstrate that such an intuitive, photonic crystal inspired approach enables achieving more than 95% absorptivity in the frequency range from 400 GHz to 1.2 THz by using a 200 nm thick "bubble wrap" polymer nanomembrane covered with graphene. The developed diffraction theory perfectly explains our experimental findings by taking into account holes and defects in the bubble wrap nanomembrane as well as the variation of the

* Corresponding author. Department of Physics and Mathematics, Institute of Photonics, University of Eastern Finland, P.O. Box 111, FI-80101, Joensuu, Finland.
E-mail address: polina.kuzhir@uef.fi (P. Kuzhir).
[1] Contributed equally.
[2] Abbreviations: THz – Terahertz, EM – electromagnetic, CVD – chemical vapor deposition, PMMA – poly-methyl methacrylate.

https://doi.org/10.1016/j.carbon.2021.09.067

attached graphene layers number over the surface. Moreover, the performed numerical simulation shows the high robustness of the metasurface, which is capable to provide nearly perfect broadband absorption when up to 40% of hemispheres that comprise its surface are damaged.

2. Materials and methods

2.1. Metasurface fabrication

Fig. 1 sketches fabrication flow of the all-graphene metasurface. At first the array of the polymer hemispheres with 490 μm diameter and 600 μm period was 3D printed on silica substrate *(step 1)* as described in Ref. [8]. In brief, we use a custom-made inkjet printer equipped with multi-nozzle printheads. Each nozzle can deposit 17 μm in diameter droplets of liquid polymer (Opticlear© by Luxexcel) on the substrate. Adjacent droplets merge before UV curing, forming as a layer of wanted shape and thickness of around 4.1 μm on the SiO_2 substrate. The next layer is added on the top of the previous one and such a layer-on-layer process is repeated until required thickness of the polymer is achieved.

In the next step the array of polymer hemispheres was spin coated with 100 nm thick poly-methyl methacrylate (PMMA) layer *(step 2)*, which is sputtered by 30 nm thick layer of Ni *(step 3)*. After that the thickness of the nickel was increased to 300 μm by electroplating *(4 step)* to make the Ni template suitable for further CVD graphene synthesis. For electroplating we used nickel sulfamate solution at +40 °C temperature as an electrolyte. The Ni layer on the PMMA membrane acts as a cathode and the electroplated nickel will accumulate making the sputtered layer thicker. The negative pole of the DC current source is connected to the sputtered nickel layer by pressing the sample against a stainless-steel contact ring. At the start of the process the current is ramped up until 4A is reached. The final thickness of Ni template and the amount of transferred nickel were monitored by measuring the electric charge flown between electrodes.

After lift-off in acetone *(step 5)*, the Ni surface imprinted with hemispheres array was placed in the chemical vapor deposition (CVD) chamber (Carboline Gero CTF 12/75/700) to grow graphene using the methane as carbon precursor *(step 6)*. The 1 cm × 1 cm Ni template was heated to 900 °C at the rate of ~20 °C/min under 20 sccm hydrogen flow. After waiting for 1 h at that temperature CH_4 at 40 sccm was introduced into the chamber and graphene layer was grown on Ni template surface for 30 min. Then CH_4 flow was shut off, the chamber was filled with hydrogen (the pressure 5 mbar) and cooled down to the room temperature.

Finally, the corrugated Ni surface covered by the graphene layer was spin-coated with 200 nm PMMA, and the Ni catalytic support has been etched out *(step 7)*. The obtained bubble wrap graphene/PMMA membrane was transferred to the Kapton support with a hole 0.7 cm × 0.7 cm. Since the 200 nm thick PMMA is invisible for the THz radiation [9,10] having almost frequency independent refractive index of n = 1.6 and low absorption coefficient (α = 3.56 cm^{-1} at frequency of 1 THz), the free-standing bubble wrap membrane can be seen as all-graphene THz metasurface.

2.2. Structural characterization

Raman spectra were collected by Raman Microscope (Renishaw, UK) with 514 nm laser at 20 × -50 × magnification and 2 mW of laser power exposed for 10 s. Scanning electron microscope SEM - LEO 1550 Gemini was used to characterize the graphene as grown on Ni template and the free standing all-graphene metasurface. Morphology of the membrane was studied by Kelvin Probe Force Microscopy using Atomic Force Microscope (AFM) MultiMode 8 (Bruker, USA) equipped with Antimony (n) doped Silicon probe (25 nm tip radius, 0.28 N/m stiff coefficient and 10 kHz resonant frequency) coated with PtIr.

2.3. THz characterization

THz time-domain spectrometer (T-Spec, EKSPLA, Vilnius, Lithuania) was used for the THz transmittivity and reflectivity measurements. THz beam was generated and detected by the low temperature grown GaBiAs photoconductive antenna, which was excited by femtosecond laser with an emission wavelength of 1050 nm, pulse repetition rate 80 MHz and duration 150 fs. The gold-coated parabolic mirrors were used to focus and collimate the incident THz beam on the sample surface. The diameter of beam spot at the focal point of the parabolic mirror was about 3–4 mm. To analyze the dependence of transmittivity on the angle of incidence the sample was placed on the rotation stage. To improve the signal to noise ratio, the 1024 scanned curves were averaged for each measurement. Fast Fourier transformations were performed to convert the time-domain signal into the frequency-domain. The THz radiations were incident from the convex side of the hemispheres.

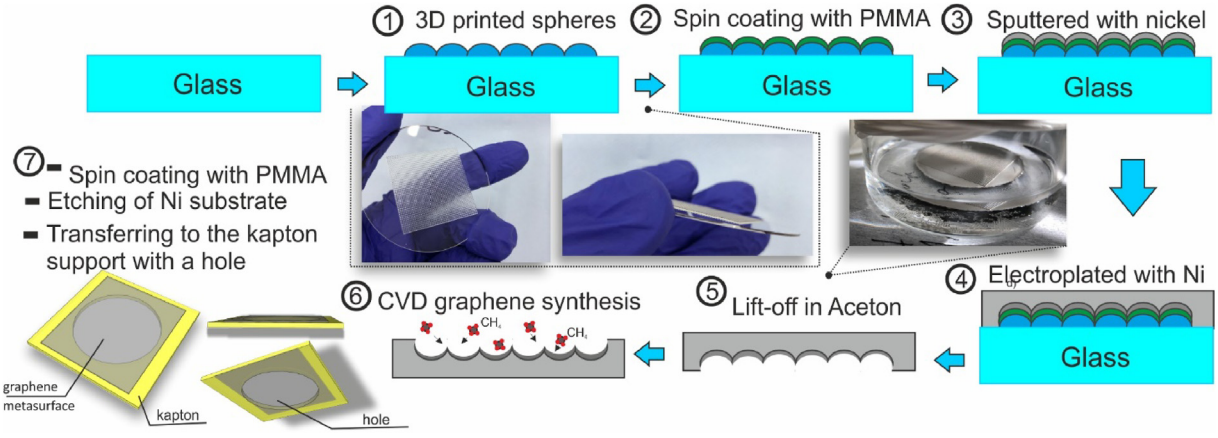

Fig. 1. The sketch of the fabrication flow of free-standing graphene metasurface. (A colour version of this figure can be viewed online.)

3. Results

3.1. Experimental

One can observe from Fig. 2 that there exist defects in the graphene layer both as grown on the Ni template (see Fig. 2a and b), and attached to the "bubble wrap" polymer nanomembrane after Ni catalyst etching (Fig. 2c). The latter show both partly immersed volcanic-type defects (see sketch in Fig. 5a) where hemispheres has collapsed forming of moon-like craters and even microscopic holes.

The surface has patch-type structure, composed of graphene areas marked as points 1, 2, 3 (Fig. 3a) easily visible by 'color' (light grey, grey, and dark grey). Fig. 3b presents most typical Raman spectra collected from the both flat and hemispherical areas. The Raman spectra reveal that metasurface is covered by a few-layered polycrystalline graphene, up to 6 layers. This corresponds to the results of the AFM measurements, showing that the average thickness of the membrane was approximately 215 nm, i.e. 200 nm thick PMMA film coated with several graphene layers. The macroscopic relief of hemispheres does not influence the patch-type surface composition: all types of graphene material in terms of number of layers and its quality (points 1, 2, 3, Fig. 3a) are presented both in the hemispherical parts of the sample and on the flat ones. The morphology of the flat and quasi-spherical parts of the all-graphene metasurface is shown in Fig. 3c and d, respectively. Fig. 3e shows volcanic-type defect, which is visible as a substantial potential gap between top and bottom sides of the settled down hemispheres. One can observe that the height difference in the corrugated area is much higher and the surface is rougher than those on the flat part of the sample. It is worth noting that small carbon particles are also observed on the membrane surface (Fig. 3 d).

Since nearly zero THz transmittivity (see Fig. 4a) and zero reflectivity was observed, we conclude that the fabricated metasurface demonstrate almost perfect absorption in the broad THz range spanning over more than one decade from 100 GHz. It is worth noting that the obtained transmittivity is four times lower than that can be achieved in the flat free standing graphene sheet of the same conductivity. Fig. 4b shows that the THz transmittivity decreases with increasing the angle of incidence.

4. Theory and numerical analysis

Negligible transmission and reflection as well as almost perfect absorption of EM radiation can be associated with the excitation of dark modes of the graphene metasurface. Usually, the dark mode originates from the hybridization of two eigenmodes that manifest itself as the Fano-like reflectivity spectrum, in which the maximum and minimum correspond to the bright and dark modes, respectively. The plasmon dark mode is associated with the out-of-phase oscillation of conduction electrons over the surface [11,12]. The excitation of the dark plasmon mode in metal nanostructures has been proposed to generate hot electrons [13] and to achieve perfect absorption [14] in a narrow frequency range.

Incident EM wave induces surface electric current density $\mathbf{j} = \sigma_s \mathbf{E}_t$, where σ_s is the graphene surface conductivity and $\mathbf{E}_t$ is the tangential component of the electric field. The surface dipole moment of the unit cell $\mathbf{d} = i\omega^{-1}\mathbf{j}$ can be presented as $\mathbf{d} = \mathbf{d}_1 + \mathbf{d}_{\mathrm{hs}}$, where $\mathbf{d}_1$ and $\mathbf{d}_{\mathrm{hs}}$ are associated with flat and hemispherical part of the unit cell, respectively. Since the hemisphere has a finite height, the tangential component of the incident electric field at the hemispherical part of the unit cells and, correspondingly, $\mathbf{d}_{\mathrm{hs}}$ will be position dependent. To compare the contributions of the dipole moments $\mathbf{d}_1$ and $\mathbf{d}_{\mathrm{hs}}$ to the generated field in far zone we can consider only in-plane component of $\mathbf{d}_{\mathrm{hs}}$, i.e. $\mathbf{d}_2 = \mathbf{d}_{\mathrm{hs}} - \mathbf{n}(\mathbf{n}\,\mathbf{d}_{\mathrm{hs}})$, where $\mathbf{n}$ is the unit vector of the metasurface normal (see Fig. 5a). If dipole moments generated on the flat and hemisphere parts of the bubble wrap nanomembrane are compensated (out of phase oscillation of electrons), the EM filed in the far field vanishes indicating appearance of the dark plasmon mode. Such a dark mode is governed by the geometry of the unit cell and possesses a broadband character.

In order to visualize the formation of the dark mode, we consider electric dipoles $\mathbf{d_1}$ and $\mathbf{d_2}$ (see Fig. 5a) induced by the incident plane wave due to oscillations of the free carries situated in flat and semispherical surfaces, respectively. To compare the contributions of both dipoles on the same footing we will project the currents at hemisphere's surface onto the plane of the flat graphene at $z = 0$. The surface current density can be calculated using Ohm's law as $\mathbf{j} = \sigma_s \mathbf{E}_t$, where σ_s is the graphene surface conductivity and $\mathbf{E}_t$ is the tangential electric field of the incident radiation at the graphene surface. It is worth noting that the phase of the current density will be different for the flat and semispherical sections of graphene.

Fig. 5b demonstrates distribution of the electric current density within the unit cell of the free-standing graphene metasurface irradiated with linearly polarized along y-axis EM wave. Semi-analytical calculations based on the model presented in Methods show that y-component of the current density flowing along the flat area and hemisphere have opposite signs. Thus, by choosing appropriate radius of the hemisphere one can achieve zero dipole moment of the unit cell, i.e. the excitation of the non-radiating dark plasmon. The dark mode is remarkably broadband due to the weak non-resonant frequency dependence. Dark plasmon is characterized by near fields that vanish exponentially away from the metasurface. The current density lines resemble those of a solenoid and,

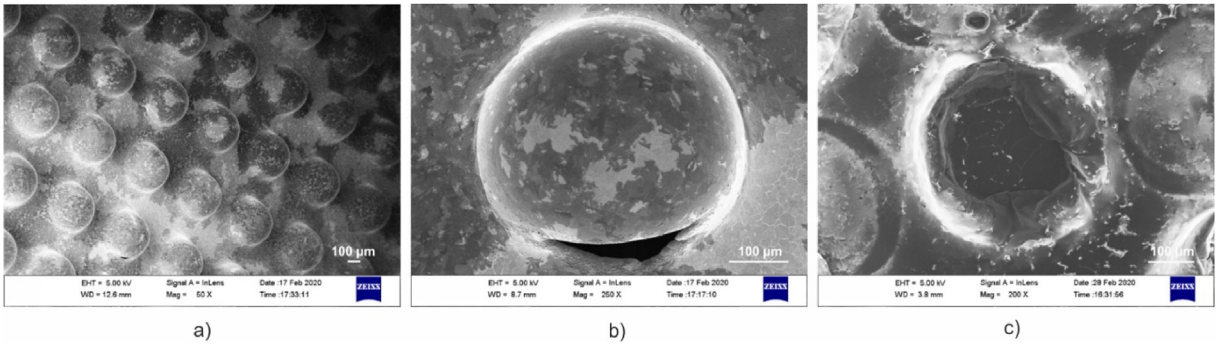

Fig. 2. SEM images of graphene hemispheres synthesized on Ni template before Ni etching (a), the same at higher magnification (b), free standing all-graphene metasurface ("bubble wrap" polymer nanomembrane covered with graphene), defected area (c). (A colour version of this figure can be viewed online.)

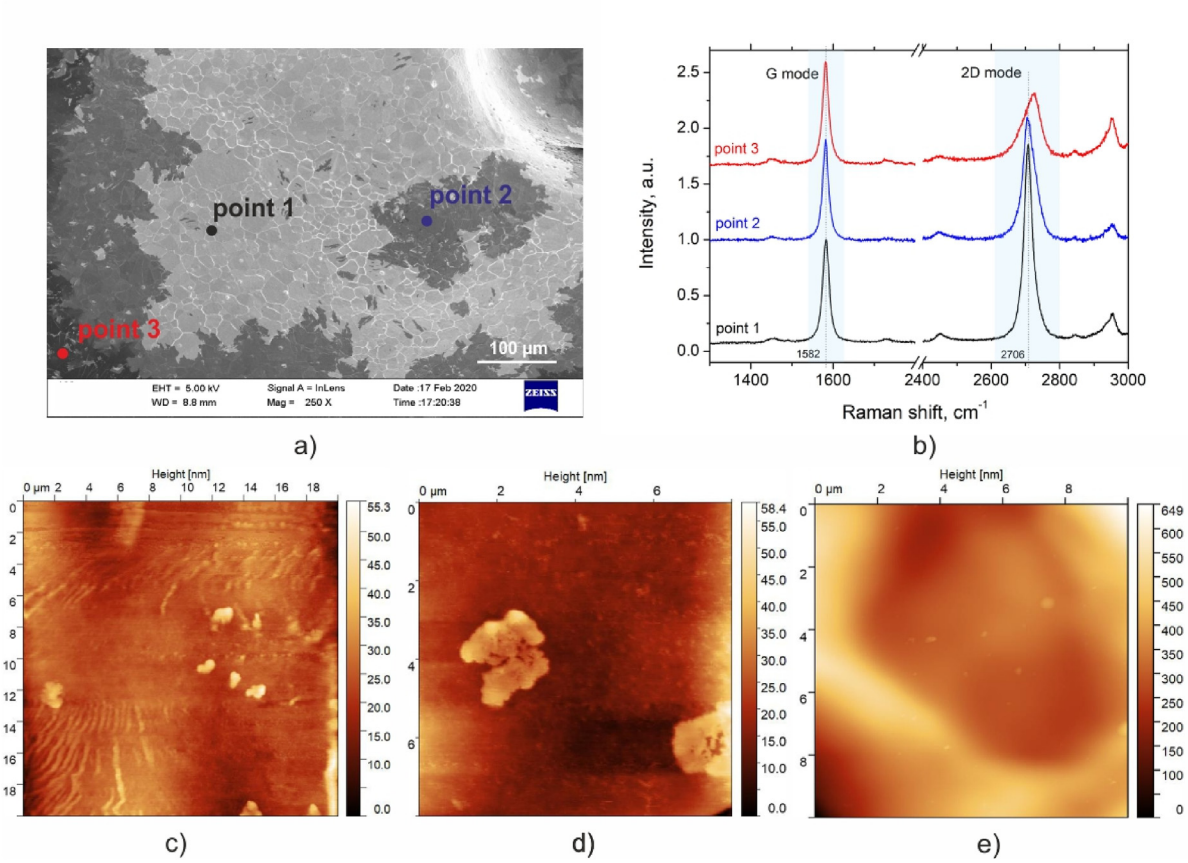

Fig. 3. (a) SEM images of all-graphene metasurface indicating the areas where the Raman spectra shown in (b) were collected. AFM images of "bubble wrap" polymer nanomembrane covered with graphene multilayers: (c) flat surface; (d) hemisphere; (e) volcanic-type structure. (A colour version of this figure can be viewed online.)

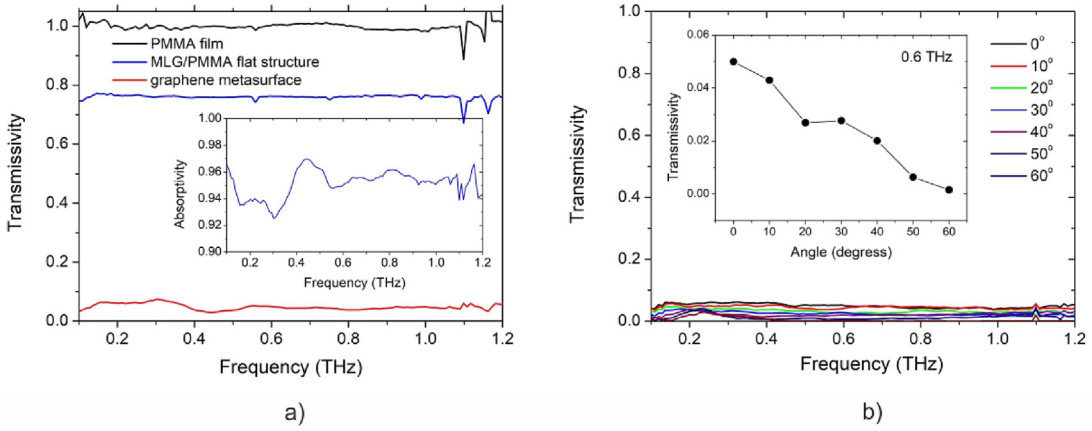

Fig. 4. a) Measured spectra of the transmittivity of the all-graphene metasurface (black solid line) and flat graphene sheet (blue solid line) at normal incidence. The insert shows the experimentally obtained absorptivity spectrum. b) Transmittivity spectra of the graphene metasurface measured at several angles of incidence. Inset shows transmittivity of the graphene metasurface at the frequency of 0.6 THz as a function of the incidence angle. Size of the unit cell $L = 611$ μm and radius of the hemisphere $r = 250$ μm. (A colour version of this figure can be viewed online.)

similar to the solenoid, most of the field is inside the system. Then the energy stored by the metasurface is the energy needed to set the stationary state. Current density is discontinuous owing to the sharp boundary between the flat graphene and hemisphere.

In order to qualitatively describe the EM properties of the metasurface, we will use the Drude model for graphene surface conductivity [15].

$$\sigma_s = \frac{Y\sigma_0}{1 + i\omega\tau} \tag{1}$$

where $\sigma_0 = e^2 E_F \tau / \pi\hbar^2$ is the static surface conductivity of the single-layer graphene, $\tau = \mu\hbar\sqrt{n_s\pi}/ev_F$ is the carrier relaxation and Y accounts for the graphene layering. We consider a simple model assuming randomly distributed 1-layer, 2-layer and 3-layer

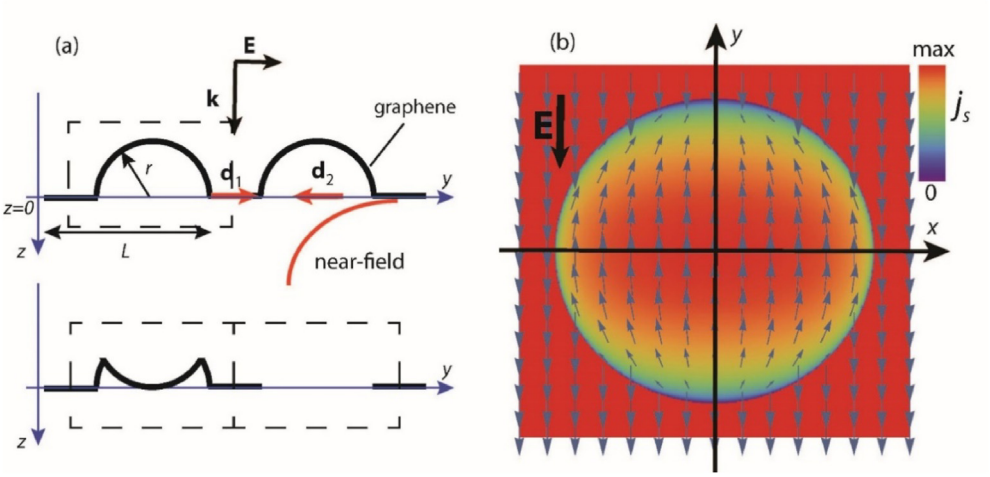

Fig. 5. Incident radiation induces counter-directed dipole moments. (a) Geometry of the graphene metasurface and incident plane EM wave. Size of the unit cell $L = 611$ μm and radius of the hemisphere $r = 250$ μm. With the dashed boxes we show the unit cells in the form of the perfect hemisphere (on the top), volcano and hole (on the bottom). (b) Vector distribution of the electric current densities at the hemisphere projected to the plane of the flat graphene $z = 0$. Density plot shows absolute values of the current densities. (A colour version of this figure can be viewed online.)

graphene areas having α_1, α_2 and α_3 shares of the whole surface ($\alpha_1 + \alpha_2 + \alpha_3 = 1$), respectively. Since the in-plane motion of the conduction electrons dominates the dc conductivity of graphene [2], the surface conductivity of the 2-layer and 3-layer thick graphene sheets are $2\sigma_0$ and $3\sigma_0$. Therefore, in Eq. (1) the layering can be taken into account by $Y = \alpha_1 + 2\alpha_2 + 3\alpha_3$.

The fields in the far zone can be found using the Kirchhoff diffraction theory (see Appendix [1]). Since in our experiment (see Fig. 4b), contribution of high diffraction orders is negligible, we calculated only specular reflection and transmission. In the modelling, we assume that there metasurface comprises three types of unit cells: perfect hemispheres, volcanic-type hemispheres and holes (see Fig. 5a). The shares of each of them are respectively w_1, w_2 and w_3 ($w_1 + w_2 + w_3 = 1$). One can see from Fig. 6a that the numerical simulation nearly perfectly reproduces the experimental results showing a negligible reflectivity, small transmittivity and extremely high absorptivity at frequencies up to 1.2 THz. By comparing the inset to Fig. 4b and in Fig. 6b one can see that the closed-form modelling well reproduces the dependence of the transmittivity spectra on the angle of incidence.

5. Discussion. Robustness of the perfect absorption

The effect of tremendously high broadband absorptivity can be better understood from the proposed theoretical model. Fig. 7a shows absorptivity spectra for perfect hemispheres ($w_1 = 1$), volcanic-type hemispheres ($w_2 = 1$), holes ($w_3 = 1$) and flat graphene sheet.

Expectedly the array of perfect hemispheres ($w_1 = 1$, $w_2 = w_3 = 0$) provides the neatly perfect absorptivity ranging from 96% to 99%. The metasurface comprising volcanic-type hemispheres ($w_1 = 0$, $w_2 = 1$, $w_3 = 0$) possesses absorptivity of about 60% in the whole spectral range. Such a reduction of the absorptivity can be explained by vanishing of the dark plasmon mode when the geometry of the unit cell is changed. Being highly transmissive, the array of holes ($w_1 = 0$, $w_2 = 0$, $w_3 = 1$) is capable to absorb even less than a flat graphene sheet (dashed curve).

The layering of the graphene metasurface does not play an important role. One can see from Fig. 7b that the absorptivity decreases in certain spectral ranges owing to the higher reflection losses due to the increase of the graphene surface conductivity. Although the non-ideality of the hemispheres decreases the

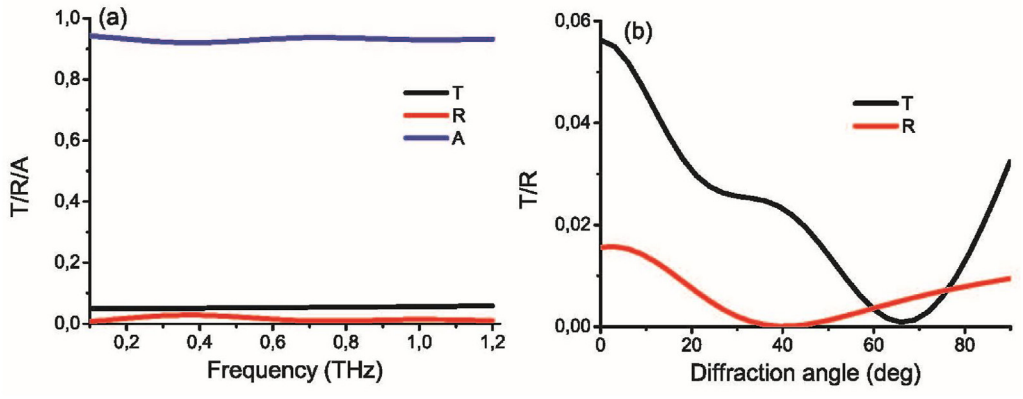

Fig. 6. Modelling results. (a) Transmissivity T, reflectivity R and absorptivity A of the modeled free-standing graphene metasurface consisting of perfect hemispheres ($w_1 = 0.6$), volcanic-type hemispheres ($w_2 = 0.35$) and holes ($w_3 = 0.05$). (b) Transmissivity T and reflectivity R as a function of incident angle at the frequency 0.6 THz. Drude-model parameters of graphene are $\mu = 1$ m^2/V, $E_F = 0.1$ eV, $v_F = 10^6$ m/s, $\alpha_1 = 0.7$, $\alpha_2 = 0.3$ and $\alpha_3 = 0$. Shares of 1-, 2- and 3-layer graphene areas are $\alpha_1 = 0.7$, $\alpha_2 = 0.3$ and $\alpha_3 = 0$, respectively. Geometrical parameters of the metasurface are $L = 611$ μm and $r = 250$ μm. (A colour version of this figure can be viewed online.)

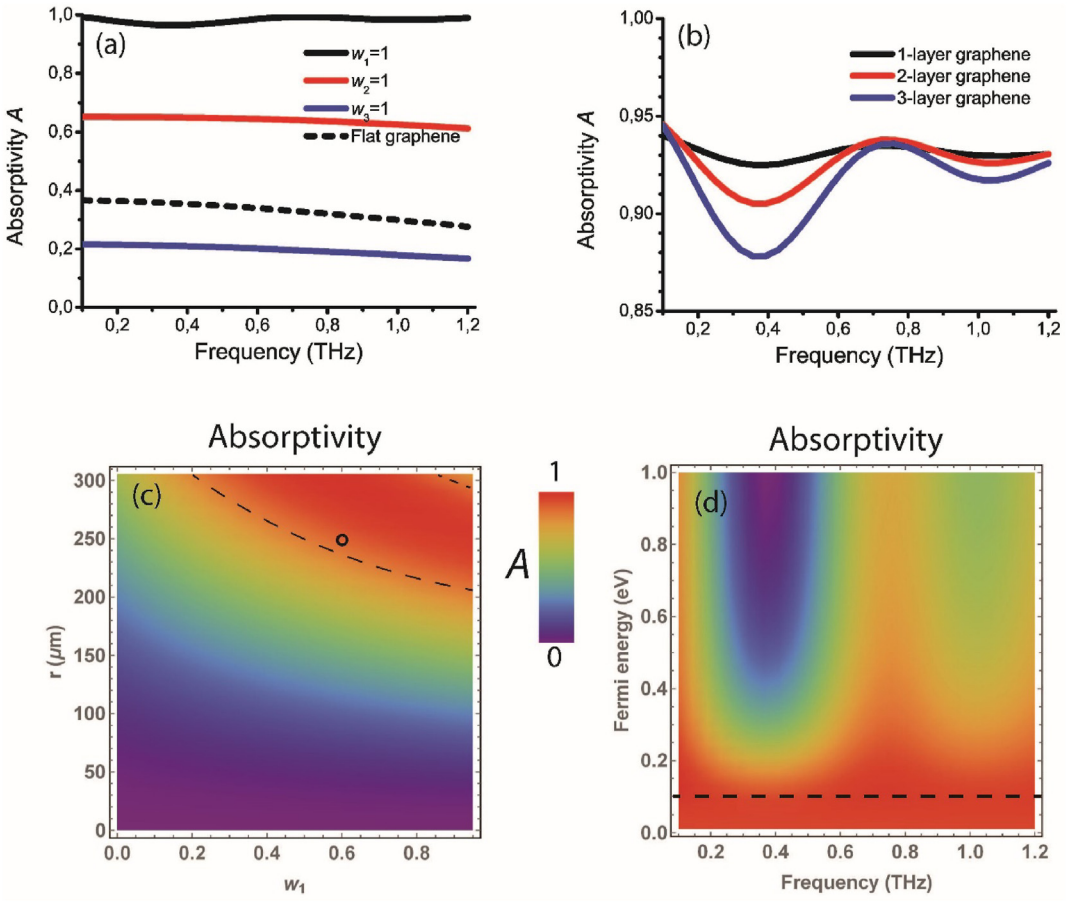

Fig. 7. Absorptivity of the free-standing graphene metasurface with parameters of Fig. 5 modeled using the Kirchhoff diffraction theory. (a) Absorption spectra for the metasurface consisting of perfect hemispheres ($w_1 = 1$), volcanic-type hemispheres ($w_2 = 1$), and holes ($w_3 = 1$). The flat graphene absorptivity spectrum is used as a reference. (b) Dependence of the absorptivity spectra on the number of graphene layers for the metasurface with the shares of cell types $w_1 = 0.6$, $w_2 = 0.35$ and $w_3 = 0.05$. (c) Absorptivity A of the single-layer graphene metasurface at the frequency of $f_0 = 0.5$ THz as a function of the weight factor w_1 and hemisphere's radius r. A share of holes is fixed to $w_3 = 0.05$, while $w_2 = 1 - w_1 - w_3$. The circle highlights metasurface parameters available from the experiment (Fig. 6). (d) Influence of the Fermi energy E_F on the absorptivity spectra of the metasurface with $w_1 = 0.6$, $w_2 = 0.35$ and $w_3 = 0.05$. The dashed line corresponds to the Fermi energy in Fig. 6a. (A colour version of this figure can be viewed online.)

absorptivity, the effect of the broken unit cells is not dramatic. According to Fig. 6 even 60% of perfect hemispheres is enough for the more than 90% absorptivity.

Fig. 7c illustrates the influence of the broken unit cells on the THz response of the metasurface. High absorptivity of the free-standing graphene metasurface can be tailored by varying the radius of hemispheres and w_1. Indeed, the dark plasmons cannot arise in the metasurface comprising small hemispeheres because the dipole moments of the flat graphene and hemisphere are not compensated. The dark plasmons can be excited if the hemisphere radius r exceeds approximately 200 μmThe dashed lines show the border of the region, in which absorptivity is above 90%. The experimental parameters fall there as well. Interestingly, the metasurface comprising perfect hemispheres does not necessarily shows the highest absorptivity. If hemisphere radius is sufficiently big, a mix of perfect and volcanic-type hemispheres can perform better in terms of absorptivity. This allows us to make a surprising conclusion that *the imperfection of the graphene metasurface can even improve the absorptivity. Such robustness makes it unprecedentedly promising because its performance is virtually insensitive to the inevitable fabrication* defects.

The Fermi energy defining the graphene doping level is another important parameter of the system. As it is shown in Fig. 7d the Fermi energy E_F should be as low as possible ensuring low reflectivity of the metasurface. From the figure one can estimate the highest Fermi energy to excite the dark plasmonic state as $E_F = 0.15$ eV. For higher Fermi energies the surface conductivity of the graphene increases making the metasurface highly reflective. The reflection spectrum is caused by the phase factors and cannot be suppressed simultaneously with the transmission. Positions of the maxima and minima of the absorptivity correspond to the positions of minima and maxima of reflectivity, respectively. These positions depend on the height of the hemispheres, that is on the radius r. From Fig. 7d we can also notice a narrow frequency band of high absorptivity near $f = 0.75$ THz that can be exploited for higher doping levels as well.

6. Conclusions

An all-graphene hemispheres-type metasurface showing extremely broadband almost perfect absorption has been fabricated using a simple and reproducible templated method involving 3D printing, spin-coating, magnetron sputtering, electroplating, graphene chemical vapor deposition and etching steps.

We demonstrate both theoretically and experimentally that the broadband perfect absorption of the metasurface requires the following conditions to be fulfilled. First, its reflectivity should be small. This can be achieved if the flat material used for fabrication of the metasurface is not highly reflective, such as, e.g. non-highly doped graphene. Second, a non-radiating dark plasmon

suppressing the transmissivity is excited owing to the compensation of the unit cell dipole moment. Thus, the high absorptivity is caused by the low reflectivity and transmissivity, while its broadband nature originates from the frequency independent excitation of the dark plasmon.

To summarize, with these findings, we prove CVD graphene to be a unique platform for a nm thick broadband absorber design and manufacturing, being robust vs different types of fabrication defects, such as macroscopic holes & volcanic type hats of the hemispherical metaatoms. Only 60% of ideal hemispheres is needed to approach to almost perfect absorption, > 90%.

CRediT authorship contribution statement

Marian Baah: Investigation, (graphene synthesis and characterization, samples fabrication). **Alesia Paddubskaya:** Investigation, (THz measurements and data analysis), Conceptualization, Visualization, (hemispheres geometrical parameters optimization). **Andrey Novitsky:** Methodology, Investigation, (electromagnetic theory, data analysis), Writing – original draft. **Nadzeya Valynets:** Investigation, (THz measurements and collecting the data). **Mukesh Kumar:** Investigation, samples fabrication, Raman characterization. **Tommi Itkonen:** Methodology, (Ni template fabrication). **Markku Pekkarinen:** Methodology, 3D printing, polymer template fabrication. **Ekaterina Soboleva:** Investigation, (AFM characterization and data analysis), and. **Erkki Lahderanta:** Investigation, (AFM characterization and data analysis). **Maria Kafesaki:** Investigation, (THz data processing), Writing – review & editing. **Yuri Svirko:** Methodology, Investigation, data acquisition, Writing – review & editing, Funding acquisition. **Polina Kuzhir:** Conceptualization, Investigation, Writing – original draft, Supervision, Funding acquisition.

Declaration of competing interest

The authors declare that they have no known competing financial interests or personal relationships that could have appeared to influence the work reported in this paper.

Acknowledgements

This work is supported by the Academy of Finland grant no. 343393, and Flagship Programme “Photonics Research and Innovation (PREIN)” decision no. 320165, Horizon 2020 grants no. 823728 (DiSetCom) P.K. is supported by Horizon 2020 grants no. 836816 (TURANDOT).

Appendix

The EM field in the vicinity of the free-standing graphene metasurface can be described by taking into account scattered secondary waves. In the framework of the vectorial Kirchhoff diffraction formula [1] the electric field in the far zone can be presented in the following form:

$$\mathbf{E}(\mathbf{r}) = \frac{ik}{4\pi}(-\mathbf{I}_1 \times \mathbf{f}_1 - I_2\mathbf{f}_1 + \mathbf{I}_3 f_2),$$

where k is the wavenumber in vacuum,

$$\mathbf{I}_1 = \int_S \mathbf{n}' \times \mathbf{E}(\mathbf{r}')ds',\ I_2 = \int_S \mathbf{n}'.\mathbf{E}(\mathbf{r}')ds',\ \mathbf{I}_3 = Z_0\int_S \mathbf{n}' \times \mathbf{H}(\mathbf{r}')ds'$$

are integrals over the unit cell area S, $\mathbf{n}'$ is the unit vector normal to the surface S and directed towards the observation region, $\mathbf{E}(\mathbf{r}')$ and $\mathbf{H}(\mathbf{r}')$ are the electric and magnetic field strengths at the surface, Z_0 is the vacuum impedance.

$$\mathbf{f}_1 = \sum_j \frac{\exp(ikr_j)}{r_j}\mathbf{n}_j,\ f_2 = \sum_j \frac{\exp(ikr_j)}{r_j}.$$

Here r_j is the distance from the unit cell j to the point of observation and $\mathbf{n}_j = \mathbf{r}_j/r_j$ is the unit vector to the point of observation.

When a plane wave normally incidents on the metasurface having rotationally symmetric unit cells, I_2 is negligible and $|\mathbf{I}_1| = |\mathbf{I}_3|$. Therefore, the magnitude of the electric field can be presented as $|\mathbf{E}| = |\mathbf{I}_1|F$, where F and $|\mathbf{I}_1|$ are determined by the metasurface lattice and geometry of the unit cell, respectively. The latter equation is applicable for the flat graphene as well. In this case, for the transmitted light we write $\left|\mathbf{E}^{(tr)}\right| = \left|\mathbf{n} \times \mathbf{E}^{(tr)}L^2\right|F$, that result in $F = L^{-2}$. Thus, the transmissivity (or reflectivity) of the metasurface reads

$$T = \frac{|\mathbf{I}_1|^2F^2}{\left|\mathbf{E}^{(inc)}\right|^2} = \frac{|\mathbf{I}_1|^2}{\left|\mathbf{E}^{(inc)}\right|^2L^4}.$$

For the graphene metasurface the normally incident wave is locally reflected and transmitted at the hemisphere surface as an obliquely incident wave. Such reflected and transmitted fields are the fields at the metasurface $\mathbf{E}(\mathbf{r}')$ and $\mathbf{H}(\mathbf{r}')$ for calculation of the reflectivity and transmissivity in the far zone. To account for the inaccuracy in fabrication of the metasurface we consider three types of unit cells (see Fig. 5a). Then the reflected field can be estimated with the vector

$$\mathbf{I}_1^{(refl)} = \mathbf{I}_1^{(flat)} + w_1\mathbf{I}_1^{(hs)} + w_2\mathbf{I}_1^{(vol)},$$

where $\mathbf{I}_1^{(flat)}$, $\mathbf{I}_1^{(hs)}$ and $\mathbf{I}_1^{(vol)}$ are the integrals over the flat part of the unit cell, hemisphere and volcanic shape. The holes contribute only to the transmitted field via the integral $\mathbf{I}_1^{(h)}$ resulting in

$$\mathbf{I}_1^{(tr)} = \mathbf{I}_1^{(flat)} + w_1\mathbf{I}_1^{(hs)} + w_2\mathbf{I}_1^{(vol)} + w_3\mathbf{I}_1^{(h)}.$$

References

[1] J.D. Jackson, Classical Electrodynamics, third ed., John Wiley& Sons, 1998.
[2] K. Batrakov, P. Kuzhir, S. Maksimenko, A. Paddubskaya, S. Voronovich, Ph Lambin, T. Kaplas, Yu Svirko, Flexible transparent graphene/polymer multilayers for efficient electromagnetic field, absorption *Scientific Reports* 4 (2014) 7191.
[3] M. Lobet, B. Majerus, L. Henrard, Ph Lambin, Perfect electromagnetic absorption using graphene and epsilon-near-zero metamaterials, Phys. Rev. B 93 (2016), 235424.
[4] K. Batrakov, P. Kuzhir, S. Maksimenko, N. Volunets, S. Voronovich, A. Paddubskaya, G. Valusis, T. Kaplas, Yu Svirko, Ph Lambin, Enhanced microwave-to-terahertz absorption in graphene, Appl. Phys. Lett. 108 (2016), 123101.
[5] A.C. Tasolamprou, A.D. Loulouklidis, Ch Daskalaki, ChP. Mavidis, G. Kenanakis, G. Deligeorgis, Z. Viskadourakis, P. Kuzhir, S. Tzortzakis, M. Kafesaki, E.N. Economou, C.M. Soukoulis, Experimental demonstration of ultrafast THz modulation in graphene-based thin film absorber through negative photoinduced conductivity, ACS Photonics 6 (3) (2019) 720–727.
[6] D.K. Efetov, R.-J. Shiue, Y. Gao, B. Skinner, E.D. Walsh, H. Choi, J. Zheng, Ch Tan, G. Crosso, Ch Peng, J. Hone, K.Ch Fong, D. Englund, Fast thermal relaxation in cavity-coupled graphene bolometers with a Johnson noise read-out, Nat. Nanotechnol. 13 (2018) 787–801.
[7] A. Blaikie, D. Miller, B.J. Alemán, A fast and sensitive room-temperature graphene nanomechanical bolometer, Nat. Commun. 10 (2019) 4726.
[8] G.A. Bisrat, M. Pekkarinen, H. Partanen, J. Biskop, J. Turunen, J. Saarinen, Imaging-quality 3D-printed centimeter-scale lens Optics Express 27 (9) (2019) 12630–12637.

[9] M. Zhai, et al., Pulsed THz imaging for thickness characterization of plastic sheet, NDT&E International 116 (2020), 102338.
[10] Y. Jin, et al., Terahertz dielectric properties of polymer, J. Korean, Phys. Soc 49 (2) (2006) 513–517.
[11] D.E. Gómez, Z.Q. Teo, M. Altissimo, T.J. Davis, S. Earl, A. Roberts, The dark side of plasmonics, Nano Lett. 13 (8) (2013) 3722–3728.
[12] B. Gallinet, O.J.F. Martin, Ab initio theory of Fano resonances in plasmonic nanostructures and metamaterials, Phys. Rev. B 83 (2011), 235427.
[13] D. Hoeing, F. Schulz, N.S. Mueller, S. Reich, H. Lange, Dark plasmon modes for efficient hot electron generation in multilayers of gold nanoparticles, J. Chem. Phys. 152 (2020), 064710.
[14] W.H. Yang, C. Zhang, S. Sun, J. Jing, O. Song, S. Xiao, Dark plasmonic mode based perfect absorption and refractive index sensing, Nanoscale 9 (2017) 8907–8912.
[15] A. Ferreira, J. Viana-Gomes, YuV. Bludov, V. Pereira, N.M.R. Peres, A.H. Castro Nero, Faraday effect in graphene enclosed in an optical cavity and the equation of motion method for the study of magneto-optical transport in solids, Phys. Rev. B 84 (2011), 235410.